Feasibility experiment and simulations for EXL

Moeini, Hossein

7. Summary and conclusions

The investigation of exotic nuclei using light-ion reactions in inverse kinematics gives access to a large domain of nuclear structure information in the region far off stability. The future FAIR facility will provide new opportunities in order to extend and advance these investigations. In particular, using stored and cooled radioactive beams in a storage ring impinging on thin internal targets enables, in comparison to investigations in inverse kinematics with external targets, high resolution measurements down to very low momentum transfers. This technique allows to deduce essential nuclear structure information that would be difficult to obtain otherwise.

Feasibility experiment

Before having the possibility to use radioactive ion beams, one was limited to use only stable or long-lived nuclei as targets. But with the advent of RIB facilities and exploiting reactions in inverse kinematics inside a storage ring, one is now able to extend the nuclear structure investigations to exotic nuclei as well. This method was applied at the ESR in a test experiment in 2005 in which a ^{136}Xe beam with an energy of 350 MeV/nucleon was stored into the ESR storage ring, continuously exposed to electron cooling and scattered off a hydrogen gas-jet target. The absolute luminosity was calculated to have reached a maximum value of $(6 \pm 2) \times 10^{27}$ cm^{-2} s^{-1}. On the detector side, we had 15 organic scintillators, each coupled to an iron converter, installed in two arrays for the detection of fast neutrons and charged particles, a position-sensitive p-i-n diode coupled to a scintillator for the identification and fast timing of the beam-like reaction products, a MWPC for the tracking of the products of atomic charge-exchange reactions, and a single-sided Si-strip detector for the detection of the low-energy recoils.

The Si-strip detector was mounted inside the UHV target chamber with the highest edge angle around 89.5° relative to the beam direction. It comprised five groups of silicon strips, each of which consisted of 8 strips. The elastic-scattering channel was studied using the first group of the Si-detector, which was the closest group to 90° in the laboratory frame. This was possible primarily because we expect a small contamination from the inelastic scattering channels for this group of the Si-detector. The thickness of the Si-detector (1 mm) was such that the elastically-scattered low-energy protons would stop in the first group of the Si-detector. This, in turn, allowed us to derive the elastic-scattering cross section using only the deposited-energy information in this group of the Si-detector (Eq. A.52). Comparing the experimental data for the elastic-scattering cross section with the simulations, we could pin down some geometrical conditions. This allowed to unfold these geometrically-imposed conditions from the available data. The simulations for the elastic scattering chan-

nel were performed making use of the calculations based on the Glauber theory as a generator for the cross section distribution. It was shown by the simulations that the interaction profile must have been an extended one, in order to be able to reproduce the elastic-scattering cross section as obtained from the experiment. However, introducing a proper extension for the interaction profile, completely compatible with what the luminosity monitors showed during the experiment, did not give the best agreement with the shape of the elastic-scattering cross section. This suggests a few scenarios. Among these scenarios is the possibility of having had interaction profiles larger than expected. Another is the wrong determination of the position or the angle of the Si-detector with respect to the center of the interaction region. The simulation results show that the effect of a larger interaction profile is equivalent to the effect of a shift in the position of the Si-detector along the beam and/or a rotation of it around the center of the interaction profile. In other words, any of the three scenarios (over-extended profile, shift in the position or rotation) could have happened during the experiment and all lead essentially to the same result in the measurement of the angular distribution of the elastic-scattering cross section.

Alternatively, one could derive the elastic-scattering cross section from the angular information of the scattered protons. However, this proved to be impossible for our experimental setup, considering the fact that the interaction profile was quite extended resulting in smoothening the spectra. Therefore, any interesting structure in the cross section pattern could not be revealed. We concluded that there is no way of precisely determining the elastic-scattering cross section, based on this approach, other than minimizing the target extension along the beam direction. In addition, even if we consider an ideal case in which we would have a point-like target, the angular method of extraction of the elastic-scattering cross section would be highly sensitive to the detector threshold. Simulations show that in order to unfold the effect of the detector threshold, when we use Fig. 5.19 to reproduce the elastic-scattering cross section, the detector position and orientation need to be measured very accurately.

Using the spectra of the deposited energy in the fifth group of the Si-detector, an attempt was made to investigate the presence of inelastic scattering events. The same method of implementing a generator for the elastic scattering channel was used to introduce an inelastic scattering channel of interest in the simulations, namely IVGDR channel with the centroid excitation energy of 15.2 MeV. Clearly, the implementation of an appropriate generator into the simulations should include the kinematics as well as the proper cross sections. Hence, by analyzing the simulation results for the fifth group of the Si-detector based on theoretical predictions for both the elastic and inelastic scattering channels, an estimate of the reaction rates for the two reaction channels could be made. This, in turn, led us to derive the proper fraction of the two channels contributing to the experimental spectra observed by the fifth group of the Si-detector. Consequently, we could estimate the contribution of the assumed inelastic scattering channel in building up the tail of the deposited energy. Based on Figs. 5.29 and 5.30, we qualitatively concluded that a combination

of two problems, a possible wrong detector calibration and/or the non-linearities in the detector response, can explain the different positions of the elastic scattering peak in the experiment as compared to the simulations. Nonetheless, comparing experiment and simulations, a clear evidence of inelastic events for GDR channel is observed in data. In conclusion, the results of the feasibility study seem to be promising and the experiment serves as an important milestone for the EXL project.

Simulations for EXL

The simulations for the EXL recoil detector setup started by constructing the forward part of the ESPA [39] in a Geant4 code. At KVI, it was then taken over by implementing the EXL calorimeter EGPA into the first code and coupling it with ROOT-based codes to easily analyze the data in a hit-level (lower than event-level) analysis. The full geometry of the major detector elements of EXL was, then, completed (Fig. 4.3) by integrating the already designed magnetic spectrometer elements [41] as well as the forward scintillator arrays into the main code.

In the simulations of the EXL calorimeter, the crystal shapes were chosen to be right rectangular prismoids; see Fig. 4.5. They were spherically arranged along two angular directions (ψ and η, as shown in Fig. 4.2) in a most optimized way, for which the center of the interaction profile would coincide with the (virtual) apex of the crystal (frustum). It turned out that it is along the ψ-direction that one would expect acceptance losses, due to introducing bigger gaps along this direction, if we require the crystals to be confined between two specific ψ-angles. Consequently, for an assembly-structured calorimeter for which we divide the ψ-range into a finite number of angular intervals, we face bigger gaps between the neighboring crystals. Using CsI for making the crystals ($\rho = 4.53$ g/cm^3), we end up with a calorimeter of $M \approx 2.9$ Tons weight.

Based on the acceptance investigations for the EXL recoil detector setup, we estimated the percentage of gaps between the calorimeter crystals to be 3.6% and 2% for the assembly-structured and non-assembly-structured calorimeter geometries, respectively. On the other hand, the efficiency of the recoil detector setup for protons averages to about 99% (for 1 MeV calorimeter threshold and considering a trigger threshold of 1 MeV) for both geometries and for thrown proton energies of more than 100 MeV (Table 4.4). It was shown that this result remains the same whether we put the crystals in air or in vacuum. Having photons as impinging particles, an average calorimeter efficiency of 98% (non-assembly-structured) and 96% (assembly-structured) for the energy range of $100 - 300$ MeV was obtained, as shown in Fig. 4.20.

In order to have a comprehensive investigation of the effect of the UHV shell on the energy resolutions for protons, simulations were performed using various shell materials and thicknesses. For this, a resolution of 50 keV was considered for individual Si-detector elements and the resolution of the calorimeter crystals was derived from the fit to the available experimental data for protons; see Fig. 4.27. It

was concluded that Kapton would be the ideal material, as compared to aluminum and stainless steel, for making the UHV shell. However, from the practical point of view, it would be easier to build the inner shell from aluminum. Based on Figs. 4.28 and 4.29, the most critical region, as far as resolution is concerned, lies between 10 to 20 MeV after punching through the shell.

Tables 3.1 and 3.2 summarize some kinematical conditions and resulting constraints on energy resolutions for the EXL recoil detector setup and for a few selected typical reactions at various incident energies. Assuming a center-of-mass energy resolution of $\sigma = 300$ keV to be achieved for the recoil particles, the expected resolutions to be observed by the recoil detector setup are, in most cases, better than the imposed resolutions in the center of mass. For a few other cases in which the particles are expected to punch through the calorimeter, one may need to consider placing a thick detector right after the calorimeter to stop these particles.

Future experiments for EXL

A simulation-based investigation was performed for a proposed experiment at the ESR with ^{56}Ni nuclei as beam, and ^{3}He and ^{4}He nuclei as target. The experiment aims at studying the (^{3}He, t) reaction channel as well as inelastic scattering channels of ISGMR and ISGDR at small scattering angles. Attempts were made to design an optimized geometry for the recoil and heavy-ion detectors to achieve optimum single and coincidence reaction rates for the (^{3}He, t) reaction channel. The investigation of this channel was done for three beam energies of 50, 200, and 400 MeV/nucleon and was focused on the low-energy branch of the kinematics. This is because one is primarily interested in low-energy tritons in the ^{56}Ni(^{3}He, t) reaction channel. Eventually, one needs to take into account and differentiate the reaction rates originating from other reaction channels like the elastic scattering channel as well as, *e.g.*, tritons with the kinematics of the high-energy branch (see Fig. 6.5). Seven DSSD elements as the recoil detector setup and two heavy-ion detector elements were introduced in the simulations, in order to cover an appreciable phase space for the two branches of the kinematics (Fig. 6.7). The estimation of the reaction rates originating from the high-energy branch was done by considering an upper limit (uniform distribution) for the respective cross sections; see subsection 6.1.2. This overestimation allowed to estimate the ratio of the reaction rates corresponding to the low- and high-energy branches (in terms of differentiating low- and high-energy-branch events). The results for the beam energy of 50 MeV/nucleon which are presented in Fig. 6.9 predict comparable amount of events (corresponding to the low-energy branch) to be detected, as compared to the reaction rates coming from the high-energy branch. Based on the derived reaction rates from simulations, one could estimate the relative errors in measuring the cross sections corresponding to the low-energy branch. Assuming a luminosity of 10^{25} cm^{-2}s^{-1} and using the singles reaction rates of DSSD (1) and (5), the relative errors in cross section after fifteen days of measurement were obtained to be less than 7% (24%) [49%] for a

beam energy of 50 (200) [400] MeV/nucleon as shown in Fig. 6.11. These statistical error sizes are expected to be attainable for the angular range between 11° and 65° (except for the interval $[31°, 41°]$ for which we would expect big uncertainties due to the loss in the geometrical acceptance). Performing the experiment at 400 MeV/nucleon seems to be rather difficult unless the luminosities are increased by an order of magnitude.

A. Relativistic kinematics for two-body interactions

A.1 Kinematics

In this appendix we discuss the two-body kinematics in the relativistic framework. While the energy-momentum conservation determines the possible configurations of outgoing particles in a collision, two arguments make kinematical considerations important. First, experiments are performed in the laboratory system (LAB) in which the target particle is at rest. Second, calculations are mostly performed in the center-of-mass (CM) frame, since the dynamics depends only on the relative motion of the colliding particles. To compare theoretical calculations with experimental results, one needs to transform from one frame to the other. To link experiments and calculations, it is necessary to find the connections between energies, momenta, angles, and cross sections in the two systems, before and after collision.

To establish these connections, we use the Lorentz transformation and conservation of energy and momentum. Although from the point of view of relativistic mechanics all coordinate systems are equal, for all practical purposes only the LAB and CM frames are of particular importance. All direct observations are in the laboratory system, so it is convenient to use it for reporting experimental results. The CM coordinate system is convenient to use, since in this system the disintegration and collision processes for two particles have the maximum degree of symmetry. Thus, for example, if there are no polarization effects, the disintegration of one particle into two others is characterized by a spherically symmetric distribution of secondary particles in the center-of-mass frame.

A.1.1 Kinematical invariants

Consider the case of two incoming particles 1 and 2 scattering to produce two outgoing particles 3 and 4 (Fig. A.1). One can define the invariant Mandelstam variables s as the square of the total energy in the CM frame, t as the square of the four-momentum transfer, and u as the crossed four-momentum transfer squared as follows:

$$\begin{aligned} s &= (p_1 + p_2)^2 = (p_3 + p_4)^2 \\ t &= (p_1 - p_3)^2 = (p_4 - p_2)^2 \\ u &= (p_1 - p_4)^2 = (p_3 - p_2)^2, \end{aligned} \tag{A.1}$$

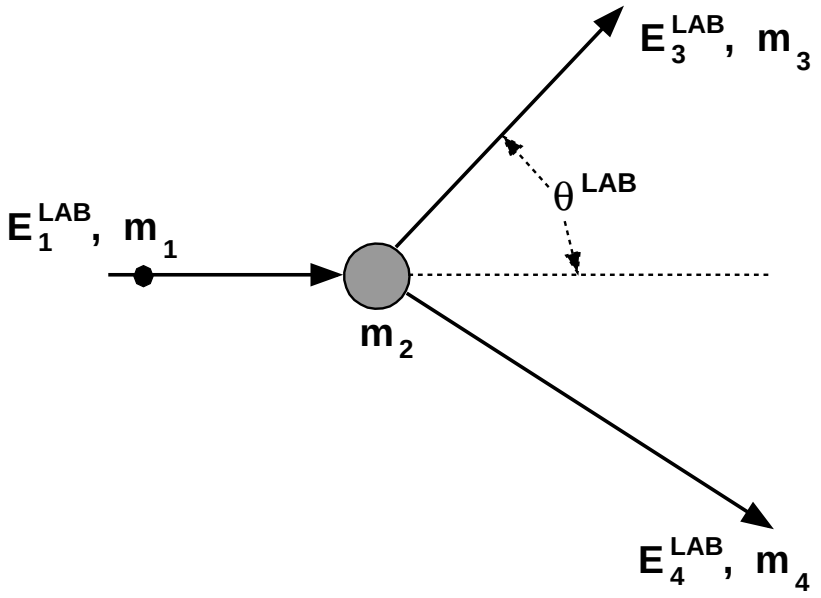

Figure A.1: Scattering variables in a typical two-body scattering. Here, m_i is the rest mass of the i^{th} particle and m_2 is considered to be at rest in LAB frame. ${E_i}^{LAB}$ represents the total energy of the i^{th} particle in LAB.

from which it follows that (we use hereafter natural units; $\hbar = c = 1$):

$$s + t + u = {m_1}^2 + {m_2}^2 + {m_3}^2 + {m_4}^2 = const., \tag{A.2}$$

which shows that only two of the three invariants are independent. Experimentally, the total energy of the beam particle in the LAB frame (${E_1}^{LAB}$), mass of the beam particle (m_1), and target-particle mass (m_2) are fixed. Thus, for given outgoing masses m_3 and m_4 and for a particular scattering angle θ^{LAB}, the corresponding energies ${E_3}^{LAB}$ and ${E_4}^{LAB}$ can be computed from the four-momentum conservation relation:

$$p_1 + p_2 = p_3 + p_4. \tag{A.3}$$

The kinematical invariant s is then given by:

$$s \equiv {(p_1 + p_2)^2}_{CM} = \left({E_1}^{CM} + {E_2}^{CM},\ 0\right)^2 = \left({E_3}^{CM} + {E_4}^{CM},\ 0\right)^2 \tag{A.4}$$

$$\equiv {(p_1 + p_2)^2}_{LAB} = \left({E_1}^{LAB} + m_2,\ \overrightarrow{p_1}^{LAB}\right)^2 = {m_1}^2 + {m_2}^2 + 2m_2{E_1}^{LAB}.$$

Similarly:

$$\begin{aligned} t &= {m_1}^2 + {m_3}^2 + 2\left(\overrightarrow{p_1} \cdot \overrightarrow{p_3} - E_1E_3\right) \\ &= {m_2}^2 + {m_4}^2 - 2m_2{E_4}^{LAB}, \end{aligned} \tag{A.5}$$

and

$$\begin{aligned} u &= {m_1}^2 + {m_4}^2 + 2\left(\overrightarrow{p_1}\cdot\overrightarrow{p_4} - E_1E_4\right) \\ &= {m_2}^2 + {m_3}^2 - 2m_2{E_3}^{LAB}, \end{aligned} \tag{A.6}$$

in which E_i and $\overrightarrow{p_i}$ are the total energy and three-momentum of the i^{th} particle in an arbitrary coordinate system.

Inserting ${E_i}^{CM} = \left(\left(\overrightarrow{p_i}^{CM}\right)^2 + {m_i}^2\right)^{1/2}$, as the total energy of the i^{th} particle in the CM frame, into the first equation of A.4, and using the relations $|\overrightarrow{p_1}^{CM}| = |\overrightarrow{p_2}^{CM}|$ and $|\overrightarrow{p_3}^{CM}| = |\overrightarrow{p_4}^{CM}|$, we can obtain the magnitude of the CM momenta as follows:

$$\begin{aligned} |\overrightarrow{p_1}^{CM}| &= \frac{1}{2\sqrt{s}}\cdot\omega\left(s, {m_1}^2, {m_2}^2\right), \\ |\overrightarrow{p_3}^{CM}| &= \frac{1}{2\sqrt{s}}\cdot\omega\left(s, {m_3}^2, {m_4}^2\right), \end{aligned} \tag{A.7}$$

with

$$\omega(x,y,z) = \sqrt{x^2+y^2+z^2-2xy-2yz-2xz}. \tag{A.8}$$

From Eqs. A.4, A.5, and A.6 for a fixed target particle in LAB (${E_2}^{LAB} = m_2$) we obtain

$$\begin{aligned} {E_1}^{LAB} &= \left(s - {m_1}^2 - {m_2}^2\right)/2m_2, \\ {E_3}^{LAB} &= \left({m_2}^2 + {m_3}^2 - u\right)/2m_2, \\ {E_4}^{LAB} &= \left({m_2}^2 + {m_4}^2 - t\right)/2m_2. \end{aligned} \tag{A.9}$$

By combining with Eqs. A.7, we obtain

$$\begin{aligned} |\overrightarrow{p_1}^{LAB}| &= \omega\left(s, {m_1}^2, {m_2}^2\right)/2m_2, \\ |\overrightarrow{p_3}^{LAB}| &= \omega\left(u, {m_2}^2, {m_3}^2\right)/2m_2, \\ |\overrightarrow{p_4}^{LAB}| &= \omega\left(t, {m_2}^2, {m_4}^2\right)/2m_2. \end{aligned} \tag{A.10}$$

Furthermore, the corresponding CM energies are deduced from Eqs. A.7 as follows:

$$\begin{aligned} {E_1}^{CM} &= \left(s + {m_1}^2 - {m_2}^2\right)/2\sqrt{s}, \\ {E_2}^{CM} &= \left(s - {m_1}^2 + {m_2}^2\right)/2\sqrt{s}, \\ {E_3}^{CM} &= \left(s + {m_3}^2 - {m_4}^2\right)/2\sqrt{s}, \\ {E_4}^{CM} &= \left(s - {m_3}^2 + {m_4}^2\right)/2\sqrt{s}. \end{aligned} \tag{A.11}$$

Therefore, using Eqs. A.5 and A.7 and the expressions for ${E_1}^{CM}$ and ${E_3}^{CM}$ from Eq. A.11, we can calculate the scattering angle in the CM frame in terms of the

kinematical invariants as follows:

$$\cos\left(\theta^{CM}\right) = \frac{\overrightarrow{p_1}^{CM} \cdot \overrightarrow{p_3}^{CM}}{|\overrightarrow{p_1}^{CM}||\overrightarrow{p_3}^{CM}|} \tag{A.12}$$

$$= \frac{s^2 + s\left(2t - {m_1}^2 - {m_2}^2 - {m_3}^2 - {m_4}^2\right) + \left({m_1}^2 - {m_2}^2\right)\left({m_3}^2 - {m_4}^2\right)}{\omega\left(s, {m_1}^2, {m_2}^2\right) \cdot \omega\left(s, {m_3}^2, {m_4}^2\right)}.$$

Similarly, for the scattering angle in the LAB frame, we obtain

$$\cos\left(\theta^{LAB}\right) = \frac{\overrightarrow{p_1}^{LAB} \cdot \overrightarrow{p_3}^{LAB}}{|\overrightarrow{p_1}^{LAB}||\overrightarrow{p_3}^{LAB}|} \tag{A.13}$$

$$= \frac{\left(s - {m_1}^2 - {m_2}^2\right)\left({m_2}^2 + {m_3}^2 - u\right) + 2{m_2}^2\left({m_2}^2 + {m_4}^2 - s - u\right)}{\omega\left(s, {m_1}^2, {m_2}^2\right) \cdot \omega\left(u, {m_2}^2, {m_3}^2\right)}.$$

It is convenient to have the functional form of the total energy of the outgoing particle $\left({E_3}^{LAB} \text{ or } {E_4}^{LAB}\right)$ versus the scattering angle in LAB. Substituting for s and u from Eqs. A.4 and A.6 into Eq. A.13, we will have

$$2\cos\left(\theta^{LAB}\right) = \frac{a{E_3}^{LAB} + b}{\sqrt{c\left(\left({E_3}^{LAB}\right)^2 - {m_3}^2\right)}}, \tag{A.14}$$

in which

$$a = 2\left({E_1}^{LAB} + m_2\right),\ b = {m_4}^2 - {m_1}^2 - {m_2}^2 - {m_3}^2 - 2m_2{E_1}^{LAB},\ c = \left({E_1}^{LAB}\right)^2 - {m_1}^2. \tag{A.15}$$

Subsequently, from Eq. A.14 we obtain

$${E_3}^{LAB} = \frac{-ab \pm 2\cos\left(\theta^{LAB}\right) \cdot \sqrt{4c^2{m_3}^2 \cdot \cos^2\left(\theta^{LAB}\right) + c\left(b^2 - a^2{m_3}^2\right)}}{a^2 - 4c \cdot \cos^2\left(\theta^{LAB}\right)}. \tag{A.16}$$

The functional form of ${E_3}^{LAB}$ versus θ^{LAB} in Eq. A.16 shows that there could be a turning point for θ^{LAB} as ${E_3}^{LAB}$ increases from zero to higher values. The angle, θ_0^{LAB}, at which the turning happens, is calculated from this expression as:

$$\theta_0^{LAB} = \cos^{-1}\left(\frac{\sqrt{a^2{m_3}^2 - b^2}}{2m_3\sqrt{c}}\right) \equiv \cos^{-1}\left(\sqrt{\frac{P}{Q}}\right), \tag{A.17}$$

with

$$P = 4\left({m_3}^2 - {m_2}^2\right)\left({E_1}^{LAB}\right)^2 + 4m_2\left({m_3}^2 - {m_2}^2 + {m_4}^2 - {m_1}^2\right)\left({E_1}^{LAB}\right) + \left(2{m_3}^2\left({m_2}^2 - {m_1}^2\right) + 2{m_4}^2\left({m_2}^2 + {m_1}^2\right) - \left({m_1}^2 + {m_2}^2\right)^2 - \left({m_3}^2 - {m_4}^2\right)^2\right)$$

and

$$Q = 4{m_3}^2\left(\left({E_1}^{LAB}\right)^2 - {m_1}^2\right). \tag{A.18}$$

Once we have ${E_3}^{LAB}$ versus θ^{LAB} (scattering angle of particle #3), we can calculate ${E_4}^{LAB}$ versus θ^{LAB} by using the following relation:

$${E_4}^{LAB} = {E_1}^{LAB} + m_2 - {E_3}^{LAB}. \tag{A.19}$$

It is of interest to calculate θ^{LAB} versus θ^{CM}. We can obtain θ^{LAB} using Eqs. A.12 and A.13:

$$\cos\left(\theta^{LAB}\right) = \cos\left(\theta^{CM}\right) \times \frac{\omega\left(s, {m_3}^2, {m_4}^2\right)}{\omega\left(u, {m_2}^2, {m_3}^2\right)} \times \left(\frac{\left(s - {m_1}^2 - {m_2}^2\right)\left({m_2}^2 + {m_3}^2 - u\right) + 2{m_2}^2\left({m_2}^2 + {m_4}^2 - s - u\right)}{s^2 + s\left(2t - {m_1}^2 - {m_2}^2 - {m_3}^2 - {m_4}^2\right) + \left({m_1}^2 - {m_2}^2\right)\left({m_3}^2 - {m_4}^2\right)}\right). \tag{A.20}$$

A.1.2 Transformation of cross sections

For a two-body reaction, $d\sigma/dt$ and $d\sigma/d\Omega$ have the relation:

$$d\sigma/dt = 2\pi\frac{d(\cos\theta)}{dt}\frac{d\sigma}{d\Omega}. \tag{A.21}$$

Using Eqs. A.12 and A.21, we get:

$$\left(d\sigma/d\Omega\right)^{CM} = \frac{1}{4\pi s}\omega\left(s, m_1^2, m_2^2\right)\cdot\omega\left(s, m_3^2, m_4^2\right)\frac{d\sigma}{dt}. \tag{A.22}$$

With the help of Eqs. A.9 and A.10, we introduce laboratory quantities and get:

$$d\sigma/dt = \frac{\pi\left(1 + \frac{E_1^{LAB}}{m_2} - \cos\theta^{LAB}\frac{E_3^{LAB}}{m_2}\frac{|\overrightarrow{p_1}^{LAB}|}{|\overrightarrow{p_3}^{LAB}|}\right)}{|\overrightarrow{p_1}^{LAB}||\overrightarrow{p_3}^{LAB}|}\left(d\sigma/d\Omega\right)^{LAB}. \tag{A.23}$$

Rewriting Eq. A.22 and using Eq. A.23 we will have:

$$\left(\frac{d\sigma}{d\Omega}\right)^{CM}_{normal} = \frac{1}{4\pi s}\cdot\omega\left(s,m_1^2,m_2^2\right)\cdot\omega\left(s,m_3^2,m_4^2\right)\left(\frac{d\sigma}{dt}\right)_{normal} \equiv \mathcal{J}_1\times\left(\frac{d\sigma}{d\Omega}\right)^{LAB}_{normal}, \tag{A.24}$$

with

$$\mathcal{J}_1 = \frac{\omega\left(s,m_1^2,m_2^2\right)\cdot\omega\left(s,m_3^2,m_4^2\right)}{4s\cdot|\overrightarrow{p}_1^{LAB}||\overrightarrow{p}_3^{LAB}|}\times\left(1+\frac{E_1^{LAB}}{m_2}-\cos\theta^{LAB}\frac{E_3^{LAB}}{m_2}\frac{|\overrightarrow{p}_1^{LAB}|}{|\overrightarrow{p}_3^{LAB}|}\right), \tag{A.25}$$

where "*normal*" stands for normal kinematics (light projectile on heavy target-particle) and $s = m_1^2 + m_2^2 + 2m_2E_1^{LAB}$. We can have the same expression for the inverse kinematics, where a heavy projectile impinges on the light target-particle (exchanging m_1 and m_2):

$$\left(\frac{d\sigma}{d\Omega}\right)^{CM}_{inverse} \equiv \mathcal{J}_{1,inv.}\times\left(\frac{d\sigma}{d\Omega}\right)^{LAB}_{inverse}, \tag{A.26}$$

with

$$\mathcal{J}_{1,inv.} = \frac{\omega\left(s_{inv.},m_2^2,m_1^2\right)\cdot\omega\left(s_{inv.},m_3^2,m_4^2\right)}{4s_{inv.}\cdot|\overrightarrow{p}_{1,inv.}^{LAB}||\overrightarrow{p}_{3,inv.}^{LAB}|}\times \left(1+\frac{E_{1,inv.}^{LAB}}{m_1}-\cos\theta_{inv.}^{LAB}\frac{E_{3,inv.}^{LAB}}{m_1}\frac{|\overrightarrow{p}_{1,inv.}^{LAB}|}{|\overrightarrow{p}_{3,inv.}^{LAB}|}\right), \tag{A.27}$$

in which $s_{inv.} = m_2^2 + m_1^2 + 2m_1E_{1,inv.}^{LAB}$ and "*inv.*" shows the respective quantity in inverse kinematics with the following numbering convention for the particles: particle #1 with mass m_2, particle #2 with mass m_1, particle #3 with mass m_3, and particle #4 with mass m_4. Hence, based on this notation, $E_{1,inv.}^{LAB}$ and $\overrightarrow{p}_{1,inv.}^{LAB}$ are the total energy of the beam particle (heavier than the target particle) and its 3-momentum in the LAB frame; $E_{3,inv.}^{LAB}$, $\overrightarrow{p}_{3,inv.}^{LAB}$, and $\theta_{inv.}^{LAB}$ are the total energy, 3-momentum, and scattering angle of the scattered light particle in the LAB frame. Using Eq. A.22 we have:

$$\frac{\left(\frac{d\sigma}{d\Omega}\right)^{CM}_{inverse}\cdot 4s_{inv.}}{\omega\left(s_{inv.},m_2^2,m_1^2\right)\cdot\omega\left(s_{inv.},m_3^2,m_4^2\right)} \equiv \frac{1}{\pi}\cdot\left(\frac{d\sigma}{dt}\right)_{inverse}, \tag{A.28}$$

which, using Eq. A.26, results in:

$$\left(\frac{d\sigma}{dt}\right)_{inverse} = \frac{\pi}{|\overrightarrow{p}^{LAB}_{1,inv.}||\overrightarrow{p}^{LAB}_{3,inv.}|} \times \left(1 + \frac{E^{LAB}_{1,inv.}}{m_1} - \cos\theta^{LAB}_{inv.}\frac{E^{LAB}_{3,inv.}}{m_1}\frac{|\overrightarrow{p}^{LAB}_{1,inv.}|}{|\overrightarrow{p}^{LAB}_{3,inv.}|}\right)\left(\frac{d\sigma}{d\Omega}\right)^{LAB}_{inverse}. \tag{A.29}$$

This result could have been intuitively concluded from Eq. A.23, in which $d\sigma/dt$ and $(d\sigma/d\Omega)^{LAB}$ are for normal kinematics.

In Eq. A.29, $\left(\frac{d\sigma}{d\Omega}\right)^{LAB}_{inverse}$ can be obtained from Eqs. A.24 and A.26, using the intuitive fact that $\left(\frac{d\sigma}{d\Omega}\right)^{CM}_{normal} \equiv \left(\frac{d\sigma}{d\Omega}\right)^{CM}_{inverse}$, (which in turn translates into $s_{inv.} \equiv s$):

$$\left(\frac{d\sigma}{d\Omega}\right)^{LAB}_{inverse} = \left(\frac{d\sigma}{d\Omega}\right)^{LAB}_{normal} \times \mathcal{J}_2, \tag{A.30}$$

in which

$$\mathcal{J}_2 = \frac{|\overrightarrow{p}^{LAB}_{1,inv.}||\overrightarrow{p}^{LAB}_{3,inv.}|}{|\overrightarrow{p}^{LAB}_{1}||\overrightarrow{p}^{LAB}_{3}|} \times \frac{\left(1 + \frac{E^{LAB}_{1}}{m_2} - \cos\theta^{LAB}\frac{E^{LAB}_{3}}{m_2}\frac{|\overrightarrow{p}^{LAB}_{1}|}{|\overrightarrow{p}^{LAB}_{3}|}\right)}{\left(1 + \frac{E^{LAB}_{1,inv.}}{m_1} - \cos\theta^{LAB}_{inv.}\frac{E^{LAB}_{3,inv.}}{m_1}\frac{|\overrightarrow{p}^{LAB}_{1,inv.}|}{|\overrightarrow{p}^{LAB}_{3,inv.}|}\right)}. \tag{A.31}$$

Using Eqs. A.29 and A.30, we obtain

$$\left(\frac{d\sigma}{dt}\right)_{inverse} = \left(\frac{d\sigma}{d\Omega}\right)^{LAB}_{normal} \times \frac{\pi\left(1 + \frac{E^{LAB}_{1}}{m_2} - \cos\theta^{LAB}\frac{E^{LAB}_{3}}{m_2}\frac{|\overrightarrow{p}^{LAB}_{1}|}{|\overrightarrow{p}^{LAB}_{3}|}\right)}{|\overrightarrow{p}^{LAB}_{1}||\overrightarrow{p}^{LAB}_{3}|}, \tag{A.32}$$

which could be rewritten, using Eq. A.23, to give:

$$\left(\frac{d\sigma}{dt}\right)_{inverse} \equiv \left(\frac{d\sigma}{dt}\right)_{normal} = \left(\frac{d\sigma}{dt}\right). \tag{A.33}$$

Therefore, we can summarize Eq. A.23 as follows:

$$\left(\frac{d\sigma}{d\Omega}\right)^{LAB}_{normal} = \left(\frac{d\sigma}{dt}\right) \times \mathcal{J}_3, \quad \left(\frac{d\sigma}{d\Omega}\right)^{LAB}_{inverse} = \left(\frac{d\sigma}{dt}\right) \times \mathcal{J}_4. \tag{A.34}$$

in which

$$\mathcal{J}_3 = \frac{|\overrightarrow{p}^{LAB}_{1}||\overrightarrow{p}^{LAB}_{3}|}{\pi\left(1 + \frac{E^{LAB}_{1}}{m_2} - \cos\theta^{LAB}\frac{E^{LAB}_{3}}{m_2}\frac{|\overrightarrow{p}^{LAB}_{1}|}{|\overrightarrow{p}^{LAB}_{3}|}\right)},$$

and

$$\mathcal{J}_4 = \frac{|\overrightarrow{p}^{LAB}_{1,inv.}||\overrightarrow{p}^{LAB}_{3,inv.}|}{\pi\Big(1+\frac{E^{LAB}_{1,inv.}}{m_1}-\cos\theta^{LAB}_{inv.}\frac{E^{LAB}_{3,inv.}}{m_1}\frac{|\overrightarrow{p}^{LAB}_{1,inv.}|}{|\overrightarrow{p}^{LAB}_{3,inv.}|}\Big)}. \tag{A.35}$$

An example

In this subsection, we will try to derive a differential cross section as function of the scattering angle for a specific channel, using the experimental data available for some other reactions and having only one experimental cross section point at one angle for our reaction of interest. For illustration we consider the reaction channel ^{56}Ni$(p,n)^{56}$Cu with an excitation energy of 4 MeV. The calculation of Fig. 6.4 gives the cross section $d\sigma/dt$ at a single point (0.1° in normal kinematics or equivalently at 0.34° and 1.96° in inverse kinematics for 50 and 200 MeV/nucleon, respectively), which is 623 and 240 mb/(GeV)^2 for 4 MeV excitation energy at the beam energies of 50 and 200 MeV/nucleon, respectively. Thus, from Eq. A.34 we will have $\big(\frac{d\sigma}{d\Omega}\big)^{LAB}_{inverse}$ = 1.308 and 0.079 mb/sr for these two energies, respectively. Having this single cross section point in inverse kinematics and exploiting the experimental cross section for ^{90}Zr(p,n) reaction in normal kinematics as shown in Fig. A.2, we attempt to derive the cross section $\big(\frac{d\sigma}{d\Omega}\big)^{LAB}_{inverse}$ for the reaction channel ^{56}Ni(p,n). The way we do this is to normalize to the experimental data. From Eq. A.34 we obtain $\big(\frac{d\sigma}{d\Omega}\big)^{LAB}_{normal}$ = 14.65 and 29.95 mb/sr for the beam energies of 50 and 200 MeV/nucleon, respectively. The normalization procedure is performed for the cross sections when represented as functions of qR, in which q is the 3-momentum transfer and R is the nuclear radius. At $\theta^{LAB}_{normal} = 0.1°$ we obtain qR = 0.341 and 0.170 GeV.fm/c for beam energies of 50 and 200 MeV/nucleon, respectively. Here, R = 4.629 fm is used as the radius of ^{56}Ni nucleus. On the other hand, for the ^{90}Zr(p,n) reaction in normal kinematics at 295 MeV proton energy and E_x = 10 MeV and $\Delta L = 0$ we have $\big(\frac{d\sigma}{d\Omega}\big)^{LAB}_{normal}$ = 2.1 and 7.26 mb/sr [27] at qR_0 = 0.341 and 0.170 GeV.fm/c, respectively, in which R_0 = 5.422 fm is the radius of ^{90}Zr nucleus (see Tables A.1 and A.3). Therefore, the normalization factors for proton beam energies of 50 and 200 MeV are obtained to be 14.65/2.1 = 6.976 and 29.95/7.26 = 4.125, respectively. Tables A.1, A.2, and A.3 show the results of the normalization procedure for the proton beam energies of 50 and 200 MeV.

Fig. A.3*a* shows the derived cross sections in normal kinematics (based on Tables A.1, A.2, and A.3) for the two beam energies. Using Eq. A.30 we can then extract the corresponding cross sections in inverse kinematics. Fig. A.3*b* compares the results of this procedure with the actual theoretical prediction for the cross sections of ^{56}Ni(p,n) reaction at beam energies of 50 and 200 MeV/nucleon in inverse kinematics. The agreement between the theoretical calculations and the extracted results is reasonable.

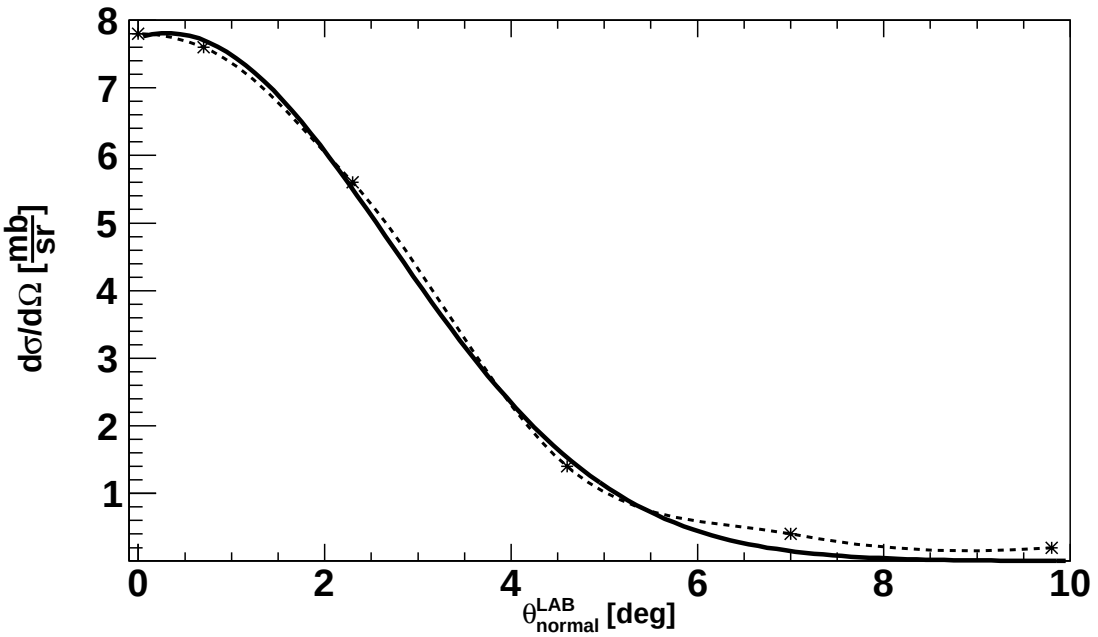

Figure A.2: Cross sections for the reaction channel $^{90}\mathrm{Zr}(p,n)$ in normal kinematics for a beam energy of 295 MeV and an excitation energy of $E_x = 10$ MeV with $\Delta L = 0$. The six data points shown here are the results of multipole-decomposition-analysis (MDA) and extracted from Ref. [27]. While the solid curve is a Gaussian fit to data points, the dotted curve is taken as the cross section in Tables A.1, A.2, and A.3, which is maximum at $\theta^{LAB}_{normal} = 0^\circ$.

A.2 Momentum-transfer analysis in $^{136}\mathrm{Xe}\,(p,p)$

For a given s, both t and u depend linearly on the $\cos\theta^{CM}$ as:

$$\begin{aligned} -t &= 2E_1^{CM}E_3^{CM} - m_1^2 - m_3^2 - 2p_1^{CM}p_3^{CM}\cdot\cos\theta^{CM} \\ -u &= 2E_2^{CM}E_3^{CM} - m_2^2 - m_3^2 - 2p_2^{CM}p_3^{CM}\cdot\cos\theta^{CM}. \end{aligned} \tag{A.36}$$

In the case of elastic scattering $\left(m_1 = m_3 \text{ and } E_1^{CM} = E_3^{CM}\right)$ and again for fixed s we can easily derive t, since it is an invariant variable which is the same in the LAB and CM frames:

$$-t = 2\left(p^{CM}\right)^2\left(1-\cos\theta^{CM}\right), \tag{A.37}$$

which has the bounds $0 \le -t \le 4\left(p^{CM}\right)^2$. Clearly, p^{CM} is the 3-vector of momentum in the CM frame and can be calculated via

$$s = \left(E_1^{CM} + E_2^{CM}\right)^2 = \left(\sqrt{m_1^2 + (p^{CM})^2} + \sqrt{m_2^2 + (p^{CM})^2}\right)^2. \tag{A.38}$$

Table A.1: Calculation of the cross section of ^{56}Ni(p,n) for 4 MeV excitation energy in ^{56}Cu in normal kinematics for $E_p = 200$ MeV through normalization to the available normal kinematics cross section of ^{90}Zr(p,n) with a beam energy of $E_p = 295$ MeV and an excitation energy of $E_x = 10$ MeV. The normalization factor at $\theta^{LAB}_{(^{56}\mathrm{Ni})} = 0.1^\circ$ was obtained to be 4.125 for this beam energy.

qR [GeV.fm/c]	$\theta^{LAB}_{(^{90}\mathrm{Zr})}$ [deg]	^{90}Zr(p,n) $(d\sigma/d\Omega)^{LAB}_{normal}$ [mb/sr]	^{56}Ni(p,n) $(d\sigma/d\Omega)^{LAB}_{normal}$ [mb/sr]	$\theta^{LAB}_{(^{56}\mathrm{Ni})}$ [deg]
0.170	1.21	7.26	29.95	0.1
0.174	1.31	7.15	29.49	0.75
0.178	1.41	7.00	28.87	1.07
0.183	1.51	6.87	28.34	1.33
0.188	1.61	6.71	27.69	1.57
0.192	1.71	6.56	27.06	1.78
0.197	1.81	6.40	26.40	1.98
0.203	1.91	6.22	25.66	2.18
0.208	2.01	6.03	24.87	2.36
0.213	2.11	5.86	24.17	2.55
0.219	2.21	5.68	23.43	2.73
0.225	2.31	5.47	22.56	2.90
0.230	2.41	5.29	21.82	3.07
0.236	2.51	5.08	20.95	3.24
0.242	2.61	4.89	20.17	3.41
0.248	2.71	4.70	19.39	3.57
0.254	2.81	4.49	18.52	3.74
0.260	2.91	4.30	17.74	3.90
0.267	3.01	4.12	16.99	4.06
0.273	3.11	3.89	16.05	4.22
0.279	3.21	3.71	15.30	4.38
0.286	3.31	3.51	14.48	4.54
0.292	3.41	3.34	13.78	4.70
0.299	3.51	3.14	12.95	4.85
0.305	3.61	2.98	12.29	5.01
0.312	3.71	2.80	11.55	5.17
0.318	3.81	2.64	10.89	5.32

Table A.2: Continued from Table A.1.

qR [GeV.fm/c]	$\theta^{LAB}_{(^{90}\mathrm{Zr})}$ [deg]	$^{90}\mathrm{Zr}(p,n)$ $(d\sigma/d\Omega)^{LAB}_{normal}$ [mb/sr]	$^{56}\mathrm{Ni}(p,n)$ $(d\sigma/d\Omega)^{LAB}_{normal}$ [mb/sr]	$\theta^{LAB}_{(^{56}\mathrm{Ni})}$ [deg]
0.325	3.91	2.47	10.19	5.48
0.332	4.01	2.31	9.53	5.63
0.338	4.11	2.18	8.99	5.78
0.345	4.21	2.03	8.37	5.94
0.352	4.31	1.88	7.75	6.09
0.359	4.41	1.76	7.26	6.24
0.366	4.51	1.63	6.72	6.40
0.372	4.61	1.52	6.27	6.55
0.379	4.71	1.40	5.77	6.71
0.386	4.81	1.29	5.32	6.86
0.393	4.91	1.20	4.95	7.01
0.400	5.01	1.10	4.54	7.16
0.407	5.11	1.01	4.17	7.31
0.414	5.21	0.93	3.84	7.46
0.421	5.31	0.85	3.51	7.62
0.428	5.41	0.78	3.22	7.77
0.435	5.51	0.70	2.89	7.92
0.442	5.61	0.65	2.68	8.07
0.449	5.71	0.59	2.43	8.22
0.456	5.81	0.54	2.23	8.37
0.463	5.91	0.48	1.98	8.52
0.470	6.01	0.43	1.77	8.67
0.477	6.11	0.40	1.65	8.82
0.484	6.21	0.36	1.48	8.98
0.491	6.31	0.32	1.32	9.13
0.499	6.41	0.29	1.20	9.28
0.506	6.51	0.26	1.07	9.43
0.513	6.61	0.23	0.95	9.57
0.520	6.71	0.21	0.87	9.73
0.527	6.81	0.19	0.78	9.88
0.534	6.91	0.16	0.66	10.03
0.541	7.01	0.15	0.62	10.17

For a frame (e.g., CM) moving along an arbitrary z-direction we have $E^{CM} = \gamma(E - vp_z)$, in which v, E, and p_z are the velocity of the frame, the particle energy, and z-component of particle momentum in the LAB (target) frame, and E^{CM} is

Table A.3: Same as Table A.1 for 50 MeV/nucleon beam energy. The normalization factor at $\theta^{LAB}_{(^{56}\mathrm{Ni})} = 0.1^\circ$ was obtained to be 6.976.

qR [GeV.fm/c]	$\theta^{LAB}_{(^{90}\mathrm{Zr})}$ [deg]	$^{90}\mathrm{Zr}(p,n)$ $(d\sigma/d\Omega)^{LAB}_{normal}$ [mb/sr]	$^{56}\mathrm{Ni}(p,n)$ $(d\sigma/d\Omega)^{LAB}_{normal}$ [mb/sr]	$\theta^{LAB}_{(^{56}\mathrm{Ni})}$ [deg]
0.341	4.15	2.1	14.65	0.1
0.345	4.21	2.03	14.16	2.41
0.352	4.31	1.88	13.11	3.95
0.359	4.41	1.76	12.28	5.06
0.365	4.51	1.63	11.37	5.99
0.372	4.61	1.52	10.60	6.81
0.379	4.71	1.40	9.77	7.56
0.386	4.81	1.29	9.00	8.25
0.393	4.91	1.20	8.37	8.91
0.400	5.01	1.10	7.67	9.53
0.407	5.11	1.01	7.05	10.12
0.414	5.21	0.93	6.49	10.70
0.421	5.31	0.85	5.93	11.26
0.428	5.41	0.78	5.44	11.79
0.435	5.51	0.70	4.88	12.32
0.442	5.61	0.65	4.53	12.83
0.449	5.71	0.59	4.12	13.33
0.456	5.81	0.54	3.77	13.82
0.463	5.91	0.48	3.35	14.31
0.470	6.01	0.43	3.00	14.78
0.477	6.11	0.40	2.79	15.25
0.484	6.21	0.36	2.51	15.71
0.491	6.31	0.32	2.23	16.17
0.499	6.41	0.29	2.02	16.63
0.506	6.51	0.26	1.81	17.07
0.513	6.61	0.23	1.60	17.52
0.520	6.71	0.21	1.46	17.95
0.527	6.81	0.19	1.32	18.39
0.534	6.91	0.16	1.12	18.82
0.541	7.01	0.15	1.05	19.25

the energy of particle in the CM frame. Alternatively, we can have the following

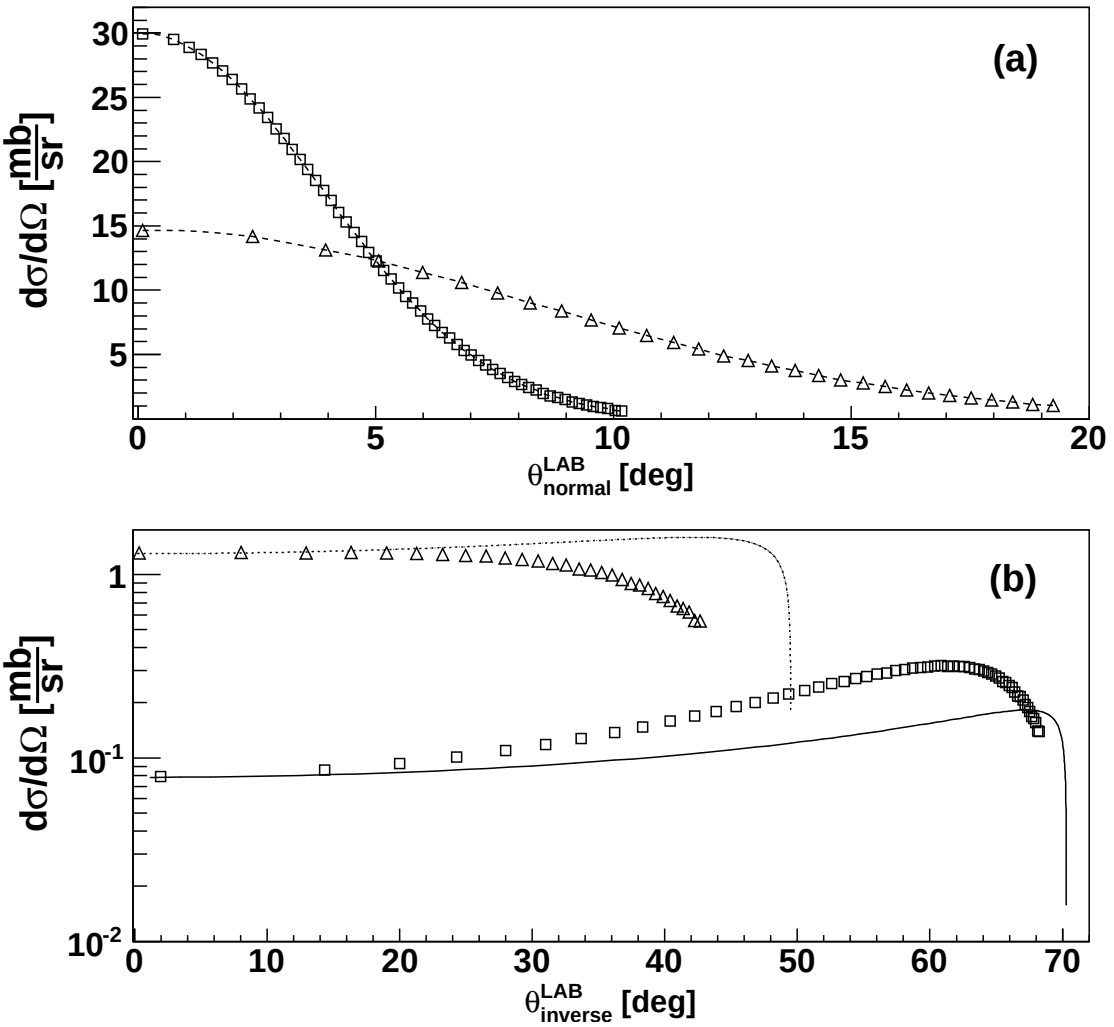

Figure A.3: (a): Cross section of the reaction channel ^{56}Ni(p, n) in normal kinematics for the proton energies of 50 (triangles) and 200 MeV (squares) and an excitation energy of 4 MeV, derived through normalization to the experimental data of Fig. A.2. (b): Theoretical prediction for the cross section in inverse kinematics for the reaction channel ^{56}Ni(p, n) with beam energies of 50 (dotted curve) and 200 MeV/nucleon (solid curve) [69]. For comparison, the extracted cross sections from the method of normalization to experimental data is also shown for the beam energies of 50 (triangles) and 200 MeV/nucleon (squares). For an extensive discussion on the derivation of the method, see the text.

transformations:

$$E = \gamma \left(E^{CM} + v p_z^{CM} \right), \; p_z = \gamma \left(p_z^{CM} + \beta E^{CM} \right), \; p_y = p_y^{CM}, \text{ and } p_x = p_x^{CM}, \quad \text{(A.39)}$$

with $\gamma = \left(1 - (v/c)^2\right)^{-1/2}$ and $c = 1$ in natural units. Consequently,

$$\tan\left(\theta^{LAB}\right) = \frac{\sqrt{p_x^2 + p_y^2}}{p_z} = \frac{\tan\left(\theta^{CM}\right)}{\gamma^{LAB}\left(1 + \frac{v \cdot E^{CM}}{p_z^{CM}}\right)}, \tag{A.40}$$

where θ^{LAB} (θ^{CM}) is the scattering angle in the laboratory (center-of-mass) frame and v is the velocity of the CM frame relative to the LAB frame (hence substituting γ and β with γ^{LAB} and β^{LAB}). For a two-body scattering, we have

$$\tan\left(\theta_i^{LAB}\right) = \frac{\tan\left(\theta_i^{CM}\right)}{\gamma^{LAB}\left(1 + \frac{v \cdot E_i^{CM}}{p_i^{CM} \cdot \cos\left(\theta^{CM}\right)}\right)}, \qquad i = 1, 2 \tag{A.41}$$

in which $|p_1^{CM}| = |p_2^{CM}| = p^{CM}$ and $\theta_2^{CM} = \pi - \theta_1^{CM}$. Therefore,

$$\tan\left(\theta_i^{LAB}\right) = \frac{\sin\left(\theta_i^{CM}\right)}{\gamma^{LAB}\left(\cos\left(\theta_i^{CM}\right) + \beta^{LAB}\frac{E_i^{CM}}{p^{CM}}\right)}, \qquad i = 1, 2 \tag{A.42}$$

The 4-momenta of the beam particle, moving in z-direction, and the target particle, fixed in LAB, can be written as

$$p_1 = (E_1, 0, 0, p_z) \quad , \quad p_2 = (E_2, 0, 0, 0) \tag{A.43}$$

Hence,

$$s = {m_1}^2 + {m_2}^2 + 2m_2\left(m_1 + K_b\right), \tag{A.44}$$

in which K_b is the kinetic energy of the beam particle in LAB. From Eqs. A.38 and A.44, we can calculate p^{CM}, β^{LAB}, and γ^{LAB}. For a ^{136}Xe beam energy of 350 MeV/nucleon, these parameters are obtained to be 0.8779 GeV, 0.6832, and 1.3695, respectively. On the other hand, from Eq. A.37, $-t$ is given by the following relations:

$$\begin{aligned} -t &= 2\left(p^{CM}\right)^2\left(1 - \cos\left(\theta_{ion}^{CM}\right)\right) \\ &= 2\left(p^{CM}\right)^2\left(1 + \cos\left(\theta_p^{CM}\right)\right), \end{aligned} \tag{A.45}$$

since in our case, the beam (ion) is moving in z-direction and the target (proton) is fixed. Therefore, we obtain

$$\tan\left(\theta_{ion}^{LAB}\right) = \frac{\sqrt{(-t) - \frac{(-t)^2}{4\left(p^{CM}\right)^2}}}{\gamma^{LAB}\left(p^{CM} - \frac{(-t)}{2p^{CM}} + \beta^{LAB}\sqrt{\left(p^{CM}\right)^2 + \left(m_{ion}\right)^2}\right)}, \tag{A.46}$$

$$\tan\left(\theta_p^{LAB}\right) = \frac{\sqrt{(-t) - \frac{(-t)^2}{4(p^{CM})^2}}}{\gamma^{LAB}\left(\frac{(-t)}{2p^{CM}} - p^{CM} + \beta^{LAB}\sqrt{(p^{CM})^2 + (m_p)^2}\right)}, \tag{A.47}$$

in which θ_{ion}^{LAB} and θ_p^{LAB} are the ^{136}Xe and proton scattering angles in LAB, and $m_{ion} = 126.5962$ GeV and $m_p = 0.9383$ GeV are their respective rest masses. We can also calculate $-t$ with respect to θ_p^{LAB} from Eq. A.42, knowing that for the elastically-scattered proton, we expect $\theta_p^{CM} > \pi/2$ (in the CM frame, the z-component of the proton momentum is negative):

$$\tan\left(\theta_p^{LAB}\right) = \frac{\sin\left(\theta_p^{CM}\right)}{\gamma^{LAB}\left(b + \cos\left(\theta_p^{CM}\right)\right)}, \tag{A.48}$$

in which $b = \beta^{LAB}\frac{E_p^{CM}}{p^{CM}} = 1$, since $p^{CM} = m_p^{CM}\beta^{LAB}$ and $m_p^{CM} \equiv E_p^{CM}$. Thus, from Eqs. A.45 and A.48 we obtain

$$-t = 4\left(p^{CM}\right)^2\left(\frac{1}{1 + \left(\gamma^{LAB}\right)^2 \cdot \tan^2\left(\theta_p^{LAB}\right)}\right). \tag{A.49}$$

It is also possible to calculate $-t$ versus the proton kinetic energy (K_p^{LAB}) after collision with the heavy ion:

$$E_p^{LAB} = \gamma^{LAB}\Big(E_p^{CM} + \beta^{LAB}p^{CM} \cdot \cos\left(\theta_p^{CM}\right)\Big), \tag{A.50}$$

with $E_p^{CM} = \sqrt{m_p^2 + (p^{CM})^2}$. Thus,

$$K_p^{LAB} = \gamma^{LAB}\Big(\gamma^{LAB}m_p + \beta^{LAB}p^{CM} \cdot \cos\left(\theta_p^{CM}\right)\Big) - m_p, \tag{A.51}$$

since before the collision, proton is assumed to be at rest $\left(E_p^{CM} = \gamma^{LAB}m_p\right)$. Thus, we obtain

$$2m_pK_p^{LAB} = 2\left(p^{CM}\right)^2\Big(1 + \cos\left(\theta_p^{CM}\right)\Big) \equiv -t, \tag{A.52}$$

using the fact that $m_p\gamma^{LAB} \equiv m_p^{CM}$.

B. The ESR internal target

The ESR internal target has become a standard device to perform in-ring experiments at the Experimental Storage Ring (ESR). There are a number of requirements to be met by the ESR internal target, which differ strongly from normal gas-jet target installations. The most critical ones are: operation under UHV conditions, no reduction of the ESR geometrical acceptance and the production of high-density targets from very different gas species. The ESR gas-jet system can deliver molecular densities of $10^{12} - 10^{14}$ cm^{-3} for various gases like He, H_2, D_2, N_2, CH_4, Ar, Kr, and Xe [70].

The main loss mechanism for highly charged ions inside the storage ring is electron capture or interaction with the residual gas. Thus, the most critical boundary condition for the operation of an internal target is the UHV system of the ESR (base pressure 10^{-11} mbar), which must remain almost unaffected. The present target philosophy can be described as creation of a supersonic gas-jet with a large number of well defined small clusters of gas. To meet the UHV requirements of the ESR, the actual setup consists of an injection and dump part, both separated by skimmers in a few stages of a differential pumping. Fig. B.1 shows a schematic view of the ESR internal target. To perform standard services without breaking the ESR vacuum, the injection part and gas-jet dump can be separated from the interaction chamber by the use of UHV compatible valves. To optimize the overlap between ESR ion-beam and target, the counting rate of photons from the interaction region, detected by a photomultiplier, is maximized by shifting the position of the ion beam. The most critical part for the formation of a supersonic gas-jet at any internal target is the vacuum stage where the gas is expanded into the vacuum. The preparation of a supersonic gas-jet with high collection speed, low temperature and small divergence, depends strongly on the geometry, the temperature, the alignment and mechanical precision of the nozzle and the first skimmer [72].

B.1 Effect of various interaction-profile shapes on the acceptance

Assuming that the drop in the elastic scattering cross section happens at $-t \approx 0.011$ (GeV/c)^2 as shown in Fig. 5.12, one can obtain the corresponding value of the proton scattering angle θ, from Eq. A.47, to be 85.32°. In the following procedure this θ value represents the angle at which the proton is generated and sent to the upper edge of the first group of the Si-detector; the generation point of the proton, say on the z-axis, is essentially where the target density (and equivalently the interaction profile) could undergo a discontinuity. The idea is to see whether or not we

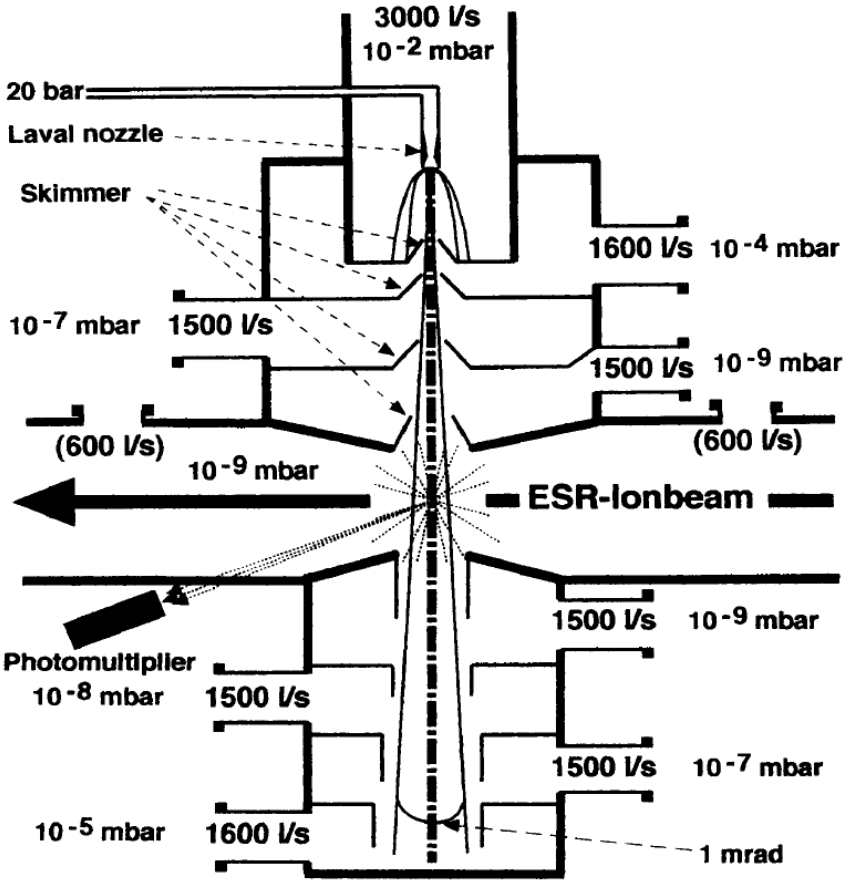

Figure B.1: Schematic picture of the ESR internal target. The jet consists of four stages at the injection and four at the dump side. The stages were pumped differentially with turbo pumps [71].

can translate back the abrupt drop in the cross section to a possible discontinuity in the pressure profile (target density). Based on the position of the first group of the Si-detector, this density discontinuity must have started at $z = -2.52$ mm, assuming the center of interaction to be at $z = 0$. Therefore, we simply assume that a pressure drop in the target must have occurred over the region of $z < -2.52$ mm. For simplicity, I proceed with assuming a discontinuity only along the z-axis, since we know that the discontinuity in the density along the x- or y-axis should have very small effect on the outcome of the simulations for the cross section. This is, of course, because of the far less impact of the derivative of the interaction profile along the latter two axes on the overall cross section, when we already see a quite small impact from the sheer extension of the interaction profile along these axes. Now I consider for the continuous part of the generation region to be a Gaussian along the z-axis, with the centroid at $z = 0$ and $\mathrm{FWHM}_z = 7.4$ mm, bounded in the interval $z \in [-2.52\ \mathrm{mm}, +\infty]$. But, for the region of $z \in [-\infty, -2.52\ \mathrm{mm}]$, we

can think of different possibilities for the generator functional form such as: uniform, damping sinusoidal or even diffraction-like patterns. Doing simulations we can study the influence of these scenarios for the shape of the interaction profile, even though it seems hard to seek physical and experimental explanations backing any of these functional forms. For $-t = 0.02$ (GeV/c)^2, we would find $z = -14.46$ mm as the lowest point (along the z-axis) from which a proton can be generated and sent to the first group of strips right at the edge of the detector located at $\theta = 89.5°$. This way, we make sure that the contribution to the cross section in the interval 0.011 (GeV/c)^2 $< -t < 0.02$ (GeV/c)^2 is solely made by the generation points in the interval $z \in [-14.46$ mm, -2.52 mm$]$. Practically, here, $z = -14.46$ mm is equivalent to $-\infty$. In order to reproduce the shape of the cross-section data, shown in Fig. 5.12, which resembles a step-like behavior at $-t \approx 0.011$ (GeV/c)^2, three functional forms were used as follows:

1) A diffraction-like pattern as sketched in Fig. B.2;

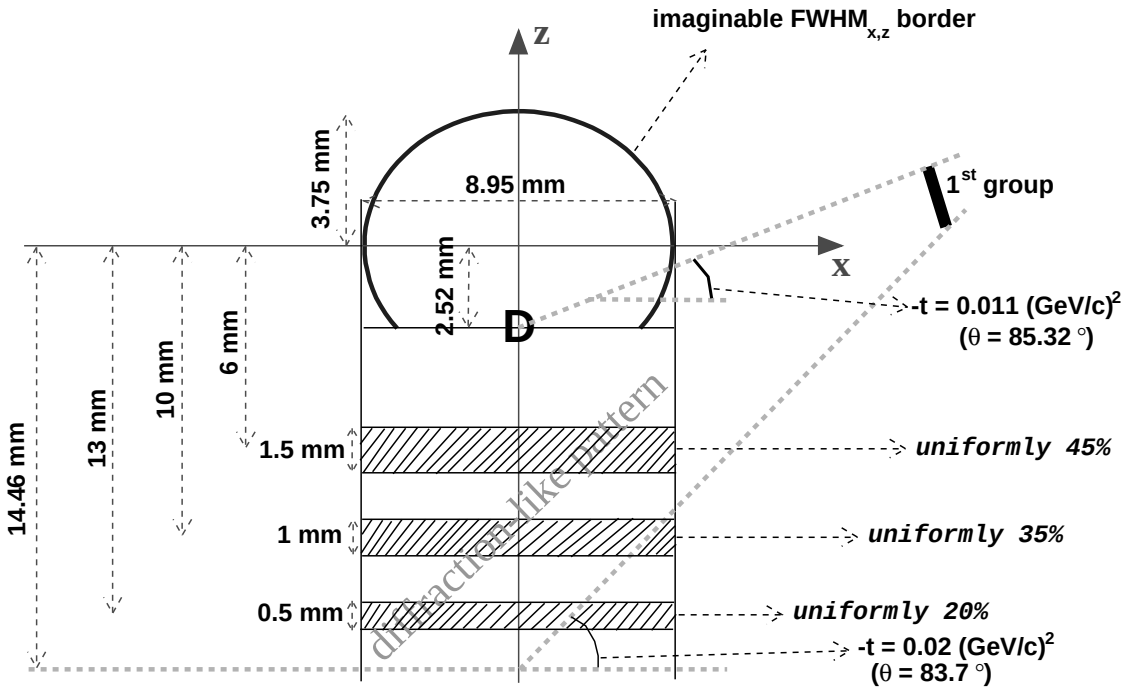

Figure B.2: An exaggerated sketch (in terms of the scales) of a diffraction-like pattern, which was assumed as the area over which the proton generation was performed for the discontinuous generation region extended from the point labeled as D down to $-\infty$ along the beam direction. The continuous Gaussian generator extends along the beam direction from D up to $+\infty$. The x- and y-components of the generation points are continuously distributed; y: uniformly, x: uniformly before and Gaussian after D along the beam direction.

2) A damping sinusoidal of the form $\frac{\sin^2(z)}{z^2}$ for generation density defined over $z \in [-\infty, -2.52$ mm$]$. The generation along the x- and y-axes was performed as continuous Gaussians of FWHM = 9 and 5 mm, respectively, all over the z-axis; and

3) A uniform function defined over $z \in [-\infty, z_0]$, followed by a gap defined over $z \in [z_0, -2.52$ mm$]$. For an optional value of $z_0 = -10$ mm, the result (Fig. B.3, bottom left panel) shows a very small enhancement around $-t = 0.013$ (GeV/c)^2.

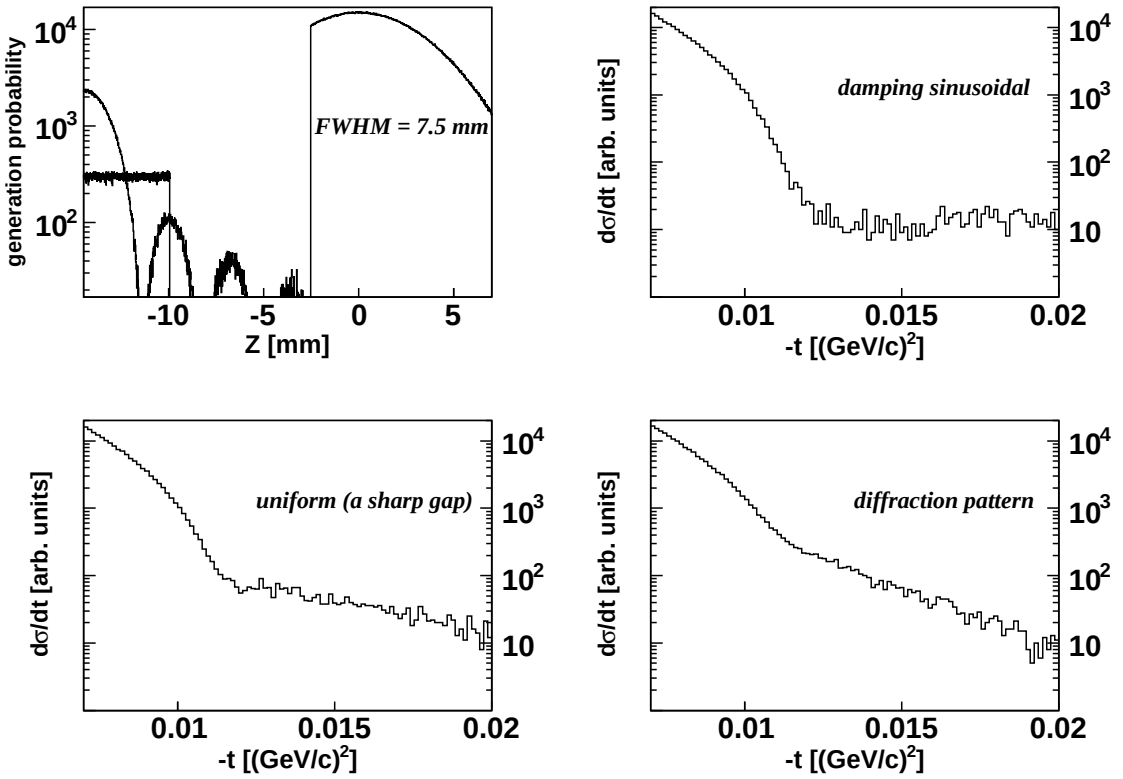

Figure B.3: Top left: functional forms (uniform and damping sinusoidal) for discontinuous generation region together with a Gaussian for the continuous generation region used as the interaction profile for particle generation along the beam direction (z-axis). The resulting shapes for elastic scattering cross section at high values of $-t$ can be compared with the one calculated based on the diffraction-like pattern (Fig. B.2).

Fig. B.3 (top left) shows the specific functional forms that were chosen for the step-like uniform and damping sinusoidal generators together with the resulting shapes for the cross section. In all the three procedures 97% of the events were dedicated to the continuous Gaussians, while 3% to the discontinuous regions. In fact, there is only a slight difference between the results of the second and third functional forms; in the case of a 'damping sinusoidal' the range of $z \in [-12$ mm$, -2.52$ mm$]$ acts effectively as a gap (see Fig. B.3, top left panel), which is a longer gap than

what I used in the 'uniform generation' approach, and that is the reason of having no enhancement around $-t = 0.013$ (GeV/c)^2. On the other hand, the high probability of generation around $z = -14$ mm, in the case of a damping sinusoidal, causes a small enhancement at very high values of $-t$ (as compared to the case of 'uniform generation'). The latter two arguments could explain the kind of fluctuations in the resulting cross section of the 'damping sinusoidal' as opposed to the one obtained for the 'step-like uniform generation'. For a generator of diffractive form, the cross section shape (Fig. B.3, bottom right panel) at higher values of $-t$ does not seem to be compatible with the experiment at all, since it has a smoothly decreasing trend rather than a uniform one (the assumption of the step-like behavior of data at high values of $-t$). This favors especially the idea of a 'gap' since, in terms of the target density distribution in the discontinuous region, the density of gas (in case of gap or damping sinusoidal) goes in the opposite direction, as compared to the assumed diffraction-like pattern, as we go to a large negative distance along the z-axis. For the discontinuous region in Fig. B.2, I optionally chose spatially uniform generation over three regions. Thus, for instance, I have only dedicated 0.6% of total events to the farthest generation region. The choice of the shape of this diffraction-like pattern should not matter, as long as we are solely interested qualitatively in studying the change in the cross section trend; based on the above discussion, the whole idea of a 'diffraction-like' interaction profile is out of question (compare Fig. B.3, bottom right panel with the experimental results in Fig. 5.12), independent of the specific form of the assumed diffractive pattern.

Apart from the different resulting shapes for the cross section in the region of large $-t$ values (Fig. B.3), what they show in common is the smoothness in their continuous spectra. Clearly, this cannot explain the broken trend of the cross section at $-t \approx 0.011$ (GeV/c)^2 as shown in Fig. 5.12. In other words, we may conclude that whatever shape the interaction profile possesses (continuous or discontinuous), it cannot explain the sudden drop in the experimental cross section. This is a valid point, since we deal with an extended interaction profile in which the contribution from different regions of the interaction profile to the cross section pattern is appreciable in smoothening any abrupt behavior originating from a discontinuous region of the interaction profile. The reason for the abrupt drop in the cross section lies most probably in the operation of the detector itself.

C. Reaction rates

An often used quantity in storage ring experiments is the integrated luminosity $\int \mathcal{L} dt$. The number of reactions which can be observed in a given reaction time is just the product of the integrated luminosity and the cross section. For a specific reaction channel, the total reaction rate is

$$\dot{N} = \mathcal{L} \cdot \int\limits_{\text{whole phase space}} (d\sigma/d\Omega)\Delta\Omega = \mathcal{L}(2\pi) \int_0^\pi (d\sigma/d\Omega) d\theta \cdot \sin\theta. \tag{C.1}$$

Considering $\mathcal{L} = x \times 10^{28}$ cm^{-2}s^{-1}, we will have $\mathcal{L} = 10x$ mb^{-1}s^{-1} which results in

$$\dot{N} = 20\pi x \int (d\sigma/d\Omega) d\theta \cdot \sin\theta, \tag{C.2}$$

where $d\sigma/d\Omega$ is given in units of mb/sr. Equivalently,

$$\dot{N} = (20\pi x) \sum_i (d\sigma/d\Omega)_i (\Delta\theta)_i \sin\theta_i, \tag{C.3}$$

in which θ_i runs over the whole phase space of the respective cross section. Choosing $(\Delta\theta)_i = 4^\circ$, we obtain

$$\dot{N} = (20\pi x)(4/180)\pi \sum_i \sin\theta_i \cdot (d\sigma/d\Omega)_i, \tag{C.4}$$

in which $(d\sigma/d\Omega)_i$ is, in principle, the mean value of every $(d\sigma/d\Omega)_j$ inside the $(\Delta\theta)_i$ at a specific θ_i.

In practice, only a fraction of all the reactions is observed by detectors. Thus, the observed reaction rate by a detector at θ_i is

$$\Delta\dot{N}_{\text{observed}} = a_i(4\pi^2/9)x \cdot (d\sigma/d\Omega)_i \cdot \sin\theta_i, \tag{C.5}$$

in which a_i ("detector acceptance") is the ratio of the number of detected light ejectiles generated at θ_i to the total number of generated light ejectiles at θ_i. Thus, the total reaction rate detected by the detector is

$$\dot{N}_{\text{observed}} = \sum_i (\Delta\dot{N})_i^{\text{observed}} = (4\pi^2/9)x \cdot \sum_i a_i (d\sigma/d\Omega)_i \cdot \sin\theta_i. \tag{C.6}$$